International Journal of Mechanical Sciences 235 (2022) 107704

Contents lists available at ScienceDirect

International Journal of Mechanical Sciences

journal homepage: www.elsevier.com/locate/ijmecsci

An explicit immersed boundary-reconstructed thermal lattice Boltzmann flux solver for thermal–fluid-structure interaction problems

Buchen Wu [a,b], Jinhua Lu [e], HsuChew Lee [b], Chang Shu [a,*], Minping Wan [b,c,d,**]

[a] Department of Mechanical Engineering, National University of Singapore, 10 Kent Ridge Crescent, Singapore, 119260, Singapore
[b] Guangdong Provincial Key Laboratory of Turbulence Research and Applications, Department of Mechanics and Aerospace Engineering, Southern University of Science and Technology, Shenzhen, 518055, Guangdong, China
[c] Guangdong-Hong Kong-Macao Joint Laboratory for Data-Driven Fluid Mechanics and Engineering Applications, Southern University of Science and Technology, Shenzhen, 518055, Guangdong, China
[d] Jiaxing Research Institute, Southern University of Science and Technology, Jiaxing, 314031, Zhejiang, China
[e] Department of Mechanical Engineering, Chair of Aerodynamics and Fluid Mechanics, Technical University of Munich, Boltzmannstraße 15, Garching, 85748, Germany

ARTICLE INFO

Keywords:
Thermal–fluid–structure interaction (TFSI)
Explicit immersed boundary method (EIB)
Reconstructed thermal lattice Boltzmann flux solver (RTLBFS)
Large deformation

ABSTRACT

Thermal–fluid–structure interaction (TFSI) problems involving multi-physics coupled effects are ubiquitous in natural environment and manmade devices. A novel coupling approach of the explicit immersed boundary-reconstructed thermal lattice Boltzmann flux solver (EIB-RTLBFS) is developed specifically to tackle TFSI problems, where a fractional method is introduced to solve TFSI problems in two successive steps. Firstly, the EIB is utilized to efficiently compute the velocity and temperature corrections that satisfy the Dirichlet boundary conditions on the surface of the solid domain. Secondly, RTLBFS, a weakly compressible finite volume solver with a clear mechanism to possess good numerical stability for high Rayleigh number convection problems, is employed to model the thermal flow. The EIB-RTLBFS is shown to be second-order accurate in space. Three benchmark cases, such as unsteady flow and natural convection that involves moving boundary, are used to evaluate the capability and robustness of EIB-RTLBFS for TFSI problems. Subsequently, a fully coupled thermal–fluid–structure system is established with a membrane structure governing equation, and the results demonstrate that the EIB-RTLBFS can accurately predict the nonlinear characteristics of this multiphysics system.

1. Introduction

Thermal–fluid–structure interaction (TFSI) problems have always been fascinating and attracted tremendous attention within the scientific and engineering communities, ranging from fundamental research [1–7] to applied research [8–13]. TFSI problems mainly evolve around thermal convection, fluid flow, and structure deformation, yielding a multi-physics coupled system with inherent nonlinear features. Therefore, it is difficult to establish an effective strategy to resolve the TFSI problems numerically. Most of the attention is placed on recovering the interaction process between the immersed object and the thermal flow.

TFSI problems involving complex geometries, moving boundaries, and/or large deformations still remain a challenge to numerical methods that are based on Eulerian meshes. Generally, a TFSI system can be divided into two categories, namely, the solid domain and fluid domain. The solid domain is most often solved using the Lagrangian framework based methods, while the fluid domain is solved with Eulerian mesh based methods. The coupling of the solid domain and fluid domain is then achieved through several different accurate yet efficient methods such as the arbitrary-Lagrangian–Eulerian (ALE) approach [14–17], the ghost particle coupling algorithm [18–21], and the immersed boundary method (IBM) [22–27]. Several researchers have utilized ALE method to investigate (i) the effect of a flexible wall in a lid-driven cavity on heat transfer performance [28], (ii) the effects of Rayleigh number on the elastic structure in a square cavity [29], and (iii) the influence of the amplitude of flexible beam in a square cavity on Nusselt number [30,31]. The main disadvantage of the ALE method is that it involves a tedious re-meshing process at every time step, where the process increases the computational time consumption and complicates its implementation. On the other hand, Long et al. [19,20,21] proposed an

* Corresponding author.
** Correspondence to: Department of Mechanics and Aerospace Engineering, Southern University of Science and Technology
E-mail addresses: mpeshuc@nus.edu.sg (C. Shu), wanmp@sustech.edu.cn (M. Wan).

https://doi.org/10.1016/j.ijmecsci.2022.107704
Received 12 June 2022; Received in revised form 7 August 2022; Accepted 29 August 2022
Available online 5 September 2022

attractive scheme by coupling the edge based smoothed finite element method (ES-FEM) solver with smoothed particle hydrodynamic (SPH) method that utilizes the temperature and velocity gradient smoothing technique over the edge based smoothing domain to investigate TFSI problems. While this method is suited for TFSI problems, the proposed scheme by Long et al. [19,20,21] is a pure Lagrangian scheme, which requires a large number of Lagrangian points that consumes enormous amount of virtual memory and computational time. Among these numerical approaches, IBM appears to be the most attractive method for resolving TFSI problems, owing to its simplicity and flexibility.

IBM distributes a series of Lagrangian points on the surface of a solid domain, where the physical boundary conditions are being enforced on these Lagrangian points. The physical information on the Lagrangian points then propagates back to the Eulerian meshes containing the fluid domain. Specifically, the boundary effects by the solid domain are taken into account by adding a source term in the fluid governing equations to simulate the fluid–structure interaction. There are several IBMs being widely used in literature, such as the penalty forcing scheme [32–34] and the direct forcing method [35,36]. However, these approaches evaluate the restoring force explicitly; thereby, the Dirichlet boundary condition is only approximately satisfied, which generates unphysical penetration of streamlines or isotherms across the solid domain. To eliminate these drawbacks, the boundary condition-enforced immersed boundary method is introduced by Wu and Shu [37,38] and Ren et al. [23] to accurately enforce the Dirichlet boundary condition on the surface of the solid domain. However, the boundary condition-enforced IBM involves assembling and inverting a large matrix, hampering it utilization in real-world applications. To circumvent these disadvantages, Zhao et al. [39] proposed an explicit boundary condition-enforced IBM (EIB) to avoid computing the correlation matrix to satisfy the Dirichlet boundary conditions at the Lagrangian points. It is worth mentioning here that the EIB has been demonstrated by the present authors in the past to be very suited for FSI problems involving isothermal process [40,41]. Owning to its high efficiency and accuracy, the EIB is further extended in this present work to solve TFSI problems.

In addition to the importance of fluid–solid coupling in TFSI problems, the inclusion of the thermal process is also extremely crucial to the computational efficiency. Even though the EIB efficiently simplifies the TFSI coupling procedure, a fast thermal flow solver coupled with EIB can further enhance computational efficiency. In the fluid domain, the mass, momentum and energy conservation laws should be fulfilled, resulting in Navier–Stokes (N–S) equations. The N–S equations can be solved by several numerical schemes, including the finite volume method (FVM) [42], the finite difference method (FDM) [43], and the finite element method (FEM) [44]. The commonly N–S solvers [45–47] directly discretize the incompressible governing equations from macroscopic conservation laws in the fluid domain with a high order of accuracy, but the slow convergence of the pressure-Poisson equation is unavoidable, consuming most of the overall computational time.

Alternatively, the thermal flows can be solved at the mesoscopic scale using the lattice Boltzmann method (LBM). The LBM is based on kinetic theory, hence, it governs both fluid dynamics and heat transfer. Several thermal lattice Boltzmann methods have been proposed in the literature such as the multi-speed model [48–51], the hybrid lattice Boltzmann model [52–55], and the double distribution function (DDF) model [56,57]. However, these thermal LBMs inherit the drawbacks of a traditional LBM, such as the uniformity of grids, the tie-up between time step and mesh size, and large memory requirement for distribution functions. To take the distinctive advantages of both traditional N–S solvers and thermal LBMs, Wang et al. [58,59] proposed a thermal lattice Boltzmann flux solver (TLBFS). The TLBFS adopts the FVM to solve the N–S equations but the macroscopic viscous/inviscid fluxes on the cell interfaces are obtained by reconstructing the local solution of the thermal LBM. The TLBFS have been demonstrated to work even for high Rayleigh number flows with good numerical stability and this is attributed to the additional small terms [60] found within the TLBFS. Recently, Lu et al. [60] extended the work of Wang et al. [58] and proposed the reconstructed thermal lattice Boltzmann flux solver (RTLBFS), which explicitly gives the numerical dissipation terms in macroscopic form and consequently has a clear mechanism to enhance numerical stability; thereby, RTLBFS is inherently a macroscopic model and does not need to introduce LBM-related theory and unit transformation. Therefore, RTLBFS uses real physical units to simulate flow and heat transfer, and it can be easily understood and utilized by researchers who are unfamiliar with the original LBM. In addition, Lu et al. [60] demonstrated that the RTLBFS not only has similar order of accuracy to the TLBFS, but also has superior computational efficiency to the TLBFS. Therefore, this present work adopted RTLBFS to predict the thermal flows.

1.1. Contributions

The EIB and RTLBFS are extremely efficient solvers for fluid–structure interaction and thermal–fluid flow, respectively. However, there are currently no scheme to combine these two methods to solve TFSI problems. Hence, this work proposed a novel coupling strategy for EIB and RTLBFS that are suitable for TFSI problems. Motivated by this goal, the explicit boundary condition-enforced immersed boundary-reconstructed thermal lattice Boltzmann flux solver (EIB-RTLBFS) is developed in this paper. EIB-RTLBFS is demonstrated to be capable of handing various type of TFSI problems with Dirichlet boundary condition being fulfill on the surface of the solid medium, allowing for complicated geometries, natural convection, moving boundaries, and large deformations. The EIB is firstly introduced to establish a TFSI coupling strategy in both velocity and temperature fields, enriching its applicability for TFSI problems. Besides, the dynamic shape deformations of the immersed object are taken into account in the EIB-RTLBFS, indicating that the proposed method has successfully established a two-way coupling within the TFSI system. The newly devised solver is validated with some classic TFSI problems, demonstrating its capability in accurately predicting the nonlinear features found in these multi-physics systems.

1.2. Organization

The paper is organized as follows: the governing equations of the fluid dynamics, the numerical approaches for fluid dynamics, and TFSI coupling procedures are introduced in Section 2. In Section 3, the numerical accuracy test and numerical validations of the new TFSI framework are presented. Specifically, Sections 3.2–3.4 demonstrate the capability of the EIB-RTLBFS in handling unsteady thermal flow, natural convection and moving boundary problems in thermal flows. Section 4 presents the application of the newly devised solver for simulating the 3D heated flexible membrane structure. Conclusions are provided in Section 5.

2. The mathematical model and numerical approach

In this section, the governing equations describing thermal flows and the numerical approaches are introduced. In this work, with the help of the fractional step method, the solution process of flow variables in Navier–Stokes equations is decomposed into a sequence of two steps (predictor and corrector). The RTLBFS [60] predicts the velocity and temperature fields in the predictor step without considering the presence of solid object. Subsequently, the velocity and temperature corrections on the surface of the solid domain are obtained by implementing the Dirichlet boundary conditions with EIB [39] in the corrector step.

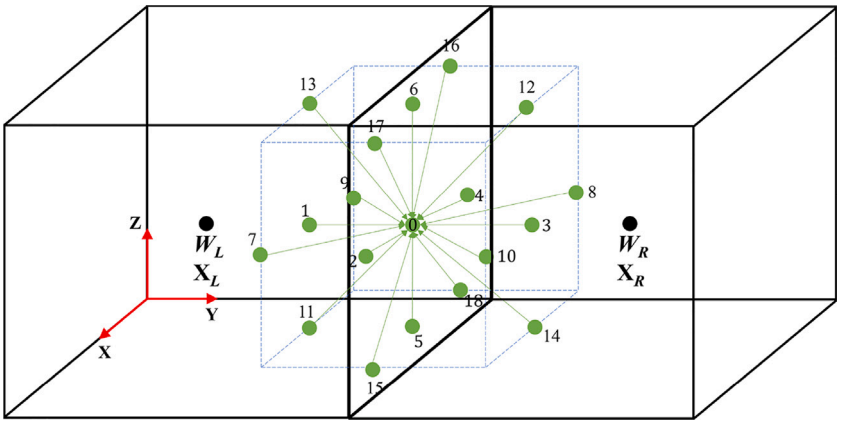

Fig. 1. Local reconstructed unit lattice D3Q19 at the cell interface. The black points denote the two adjacent cell centers and the green points represent the unit lattice points. The macroscopic flow variables at unit lattice points are approximately evaluated by the interpolation of the flow variables at the two adjacent cell centers.

2.1. Navier-Stokes (N–S) equations

The mass, momentum and energy conservation equations for general thermal viscous flows can be written as:

$$\frac{\partial \rho}{\partial t} + \nabla \cdot (\rho \mathbf{u}) = 0, \tag{1a}$$

$$\frac{\partial (\rho \mathbf{u})}{\partial t} + \nabla \cdot (\rho \mathbf{u}\mathbf{u}) = -\nabla p + \nu \nabla \cdot \left[\nabla \rho \mathbf{u} + (\nabla \rho \mathbf{u})^T\right] + \mathbf{F}_B + \mathbf{f}, \tag{1b}$$

$$\frac{\partial (\rho T)}{\partial t} + \nabla \cdot (\rho T \mathbf{u}) = \chi \nabla^2 (\rho T) + q, \tag{1c}$$

where ρ, $\mathbf{u}$, T, ν, p and χ denote the density of fluid, the flow velocity, the temperature, the kinematic viscosity, the pressure, and the thermal diffusivity, respectively. $\mathbf{F}_B = (0, 0, -\rho\zeta g(T - T_m))$ is the buoyancy force obtained with the Boussinesq approximation, where ζ, g and T_m denote the thermal expansion coefficient, gravitational acceleration and mean temperature, respectively. $\mathbf{f}$ is the external forcing term exerted by the solid system onto the fluid and the q is the heat source term indicating the heat density transferred to the fluid from the heat flux on the immersed boundary. The above N–S equations can model the dynamics of an incompressible thermal viscus fluid, when the density variation is small and Mach number is low.

2.2. The RTLBFS for determining the intermediate flow variables

In the predictor step, the standard N–S equations are solved with the RTLBFS without taking into account the solid domain; thereby, the intermediate flow variables are predicted. The governing equations shown in Eq. (1) can be expressed in a vector form:

$$\frac{\partial \mathbf{W}}{\partial t} + \nabla \cdot \mathbf{F} = 0, \tag{2}$$

where

$$\mathbf{W} = \begin{Bmatrix} \rho \\ \rho \mathbf{u} \\ \rho T \end{Bmatrix}, \quad \mathbf{F} = \begin{Bmatrix} \mathbf{P} \\ \mathbf{\Pi} \\ \mathbf{Q} \end{Bmatrix}, \tag{3a}$$

$$\boldsymbol{P} = \rho \mathbf{u}, \tag{3b}$$

$$\mathbf{\Pi} = \rho \mathbf{u}\mathbf{u} + p\boldsymbol{I} - \nu \left(\nabla \rho \mathbf{u} + (\nabla \rho \mathbf{u})^T\right), \tag{3c}$$

$$\mathbf{Q} = \rho T \mathbf{u} - \chi \nabla (\rho T). \tag{3d}$$

It should be noted that the buoyancy force $\mathbf{F}_B$ is taken into account in the intermediate step shown in Eq. (7) rather than in the flux term $\mathbf{\Pi}$.

Firstly, the RTLBFS reconstructs a unit lattice at the cell interface with D3Q19 lattice velocity model, as shown in Fig. 1. Then, the macroscopic flow variables ρ, $\mathbf{u}$ and T at each lattice node can be approximately evaluated by interpolation, and the specific interpolation scheme reads:

$$\mathbf{W} = \begin{cases} \mathbf{W}_L + \nabla \mathbf{W}_L \cdot (\mathbf{X}_N - \mathbf{X}_L), \mathbf{X}_N \text{ locates at the left cell;} \\ \mathbf{W}_R + \nabla \mathbf{W}_R \cdot (\mathbf{X}_N - \mathbf{X}_R), \mathbf{X}_N \text{ locates at the right cell;} \\ 0.5\left[\mathbf{W}_L + \nabla \mathbf{W}_L \cdot (\mathbf{X}_N - \mathbf{X}_L) + \mathbf{W}_R + \nabla \mathbf{W}_R \cdot (\mathbf{X}_N - \mathbf{X}_R)\right], \\ \qquad \mathbf{X}_N \text{ locates at the interface;} \end{cases} \tag{4}$$

where $\mathbf{X}_L$ and $\mathbf{X}_R$ denote the cell center position of the left and right cells, respectively. It should be noted that the superscripts n, $*$, m and $n+1$ denote the current, the sub-intermediate, the intermediate and the next time steps, respectively. In the case of two-dimension, the D2Q9 lattice velocity model is adopted instead.

Subsequently, the sub-intermediate flow variables ρ^*, $(\rho u_\alpha)^*$ and $(\rho T)^*$ at the cell interface are predicted by solving the macroscopic equations recovered from the local thermal LBM with the FDM method, which can be expressed as:

$$\rho^* = \rho^n - \partial_\alpha (\rho u_\alpha)^n \delta t + \frac{1}{2}\delta t^2 \partial_\alpha \partial_\beta \left(\rho u_\alpha u_\beta + \rho c_s^2 \delta_{\alpha\beta}\right)^n + O(\delta t^3), \tag{5a}$$

$$\begin{aligned} (\rho u_\alpha)^* = {} & (\rho u_\alpha)^n - \delta t \partial_\beta \left(\rho u_\alpha u_\beta + \rho c_s^2 \delta_{\alpha\beta}\right)^n \\ & + 0.5 c_s^2 \delta t^2 \partial_\beta \left[\partial_\beta (\rho u_\alpha) + \partial_\alpha (\rho u_\beta) + \partial_\gamma (\rho u_\gamma)\delta_{\alpha\beta}\right]^n + O(\delta t^3), \end{aligned} \tag{5b}$$

$$(\rho T)^* = (\rho T)^n - \delta t \partial_\alpha (\rho u_\alpha T)^n + 0.5 c_s^2 \delta t^2 \partial_\alpha \partial_\beta (\rho T \delta_{\alpha\beta})^n + O(\delta t^3), \tag{5c}$$

where subscripts α, β and γ denote the coordinate components. c_s is the speed of sound and δt is the time interval. The partial derivatives in Eq. (5) are discretized on the unit lattice using the second-order central difference scheme, and readers are referred to our previous work [61] for detailed formulations and explanation.

Through the second-order Taylor series expansion [60], the flux terms in Eq. (3a) can be simplified by invoking the macroscopic variables recovered from the local thermal LBM, which can be written as:

$$P_\alpha = (\rho u_\alpha)^*, \tag{6a}$$

$$\begin{aligned} \Pi_{\alpha\beta} = {} & \left(\rho u_\alpha u_\beta + \rho c_s^2 \delta_{\alpha\beta}\right)^* - \nu \left[\partial_\beta (\rho u_\alpha) + \partial_\alpha (\rho u_\beta) + \partial_\gamma (\rho u_\gamma)\delta_{\alpha\beta}\right] \\ & - (\tau_f - 0.5)\left[\left(\rho u_\alpha u_\beta + \rho c_s^2 \delta_{\alpha\beta}\right)^* - \left(\rho u_\alpha u_\beta + \rho c_s^2 \delta_{\alpha\beta}\right)\right] + O(\delta t^2), \end{aligned} \tag{6b}$$

$$Q_\alpha = (\rho u_\alpha T)^* - \chi \partial_\alpha (\rho T) - (\tau_g - 0.5)\left[(\rho u_\alpha T)^* - (\rho u_\alpha T)\right] + O(\delta t^2), \tag{6c}$$

where $\nu = (\tau_f - 0.5) c_s^2 \delta t$ and $\chi = (\tau_g - 0.5) c_s^2 \delta t$.

Finally, the macroscopic variables ρ^{n+1}, the intermediate flow variables $\mathbf{u}^m$, and T^m at the cell center are directly evaluated with the flux

terms as follow:

$$\rho^{n+1} = \rho^n - \frac{\Delta t}{\Delta V}\sum_k P_\alpha \Delta S_{k\alpha}, \tag{7a}$$

$$\left(\rho u_\alpha\right)^m = \left(\rho u_\alpha\right)^n + \frac{\Delta t}{\Delta V}\sum_k \Pi_{\alpha\beta}\Delta S_{k\beta} + F_{B\alpha}, \tag{7b}$$

$$(\rho T)^m = (\rho T)^n - \frac{\Delta t}{\Delta V}\sum_k Q_\alpha \Delta S_{k\alpha}, \tag{7c}$$

where ΔV is the volume of the control cell and Δt denotes the macroscopic time interval. ΔS_k denotes the area of the kth interface of the control cell. To illustrate the good numerical stability of RTLBFS at high Rayleigh number, the first-order explicit scheme is employed for the time discretization.

2.3. The EIB for evaluating the velocity/temperature corrections

The explicit boundary condition-enforced immersed boundary method is applied in the corrector step, right after the intermediate flow field is evaluated, to accurately satisfy the Dirichlet boundary conditions on the surface of the solid domain. The corrected velocity and temperature are obtained by accounting for the corrections as follow:

$$\mathbf{u}^{n+1} = \mathbf{u}^m + \Delta\mathbf{u}, \tag{8a}$$

$$T^{n+1} = T^m + \Delta T, \tag{8b}$$

where $\Delta\mathbf{u}$ and ΔT denote the corresponding corrections on the velocity and temperature fields, respectively. Therefore, the source terms in the momentum and energy equations are given as:

$$\mathbf{f} = \rho^{n+1}\frac{\Delta\mathbf{u}}{\Delta t}, \tag{9a}$$

$$q = \rho^{n+1}\frac{\Delta T}{\Delta t}. \tag{9b}$$

For simplicity, the symbol ψ is adopted to represent the velocity components and temperature, thus, Eq. (8) can be rewritten as:

$$\psi^{n+1} = \psi^m + \Delta\psi. \tag{10}$$

The difference between the local flow variables and the desired physical properties on the immersed boundary needs to be eliminated to accurately implement the Dirichlet boundary conditions, which generates the following relationship as:

$$\begin{aligned}&\psi_B\left(\boldsymbol{X}_B^l\right) = \psi^{n+1}\left(\boldsymbol{X}_B^l\right) = \sum_j \psi^{n+1}\left(\boldsymbol{r}_j\right)\cdot D\left(\boldsymbol{r}_j - \boldsymbol{X}_B^l\right)dh^3\\ &l = 1,2,\ldots,N, \quad j = 1,2,\ldots,M\end{aligned} \tag{11}$$

where the subscript B represents the Lagrangian points on the surface of the solid domain. dh is the grid spacing of the background Eulerian mesh; N and M are the numbers of Lagrangian points and Eulerian points, respectively. $\boldsymbol{r}_j$ is defined as the physical position of Eulerian points. The kernel distribution function D can be expressed as:

$$D\left(\boldsymbol{r}_j - \boldsymbol{X}_B^l\right) = \delta\left(r_j^x - X_B^l\right)\delta\left(r_j^y - Y_B^l\right)\delta\left(r_j^z - Z_B^l\right) \tag{12}$$

$$\delta(r) = \begin{cases}\frac{1}{4}(1+\cos(\pi|r/dh|/2)) & |r| \le 2dh\\ 0 & |r| > 2dh\end{cases} \tag{13}$$

The correction $\Delta\psi(\boldsymbol{r}_j)$ at Eulerian points in Eq. (10) is interpolated by the correction $\delta\psi_B^l$ at Lagrangian points as:

$$\Delta\psi\left(\boldsymbol{r}_j\right) = \sum_l \delta\psi_B^l\cdot D\left(\boldsymbol{r}_j - \boldsymbol{X}_B^l\right)\cdot\Delta s^l, l = 1,2,\ldots,N, \tag{14}$$

where Δs^l is the area of the solid boundary element. Substituting Eqs. (10) and (14) into Eq. (11), the following formula is obtained as:

$$\begin{aligned}\psi_B\left(\boldsymbol{X}_B^l\right) = &\sum_j \psi^m\left(\boldsymbol{r}_j\right)\cdot D\left(\boldsymbol{r}_j - \boldsymbol{X}_B^l\right)dh^3\\ &+ \sum_j\sum_k \delta\psi_B^k\Delta s^k\cdot D\left(\boldsymbol{r}_j - \boldsymbol{X}_B^l\right)\cdot D\left(\boldsymbol{r}_j - \boldsymbol{X}_B^k\right)dh^3.\end{aligned} \tag{15}$$

Eq. (14) can be rewritten in the matrix form as follow:

$$\mathbf{A}\boldsymbol{x} = \mathbf{B} \tag{16a}$$

$$\boldsymbol{x} = \left[\ \delta\psi_B^1\Delta s^1,\quad \delta\psi_B^2\Delta s^2,\quad \cdots,\quad \delta\psi_B^N\Delta s^N\ \right]^T, \tag{16b}$$

$$A_{ij} = \sum_{k=1}^{M} D_{ik}D_{jk}dh^3, \tag{16c}$$

$$B_i = \psi_B^i - \sum_{k=1}^{M} D_{ik}\psi_k^m \tag{16d}$$

Eq. (16) shows that the matrix term $\mathbf{A}$ is only related to the kernel function D, and Eq. (13) indicates that $D = 0$ when the relative distance between a Lagrangian point and an Eulerian point exceeds $2dh$, indicating that only the terms $A_{ij} \neq 0$ should be considered. Moreover, with the approximation of $\delta\psi_B^i\Delta s^i = \delta\psi_B^j\Delta s^j + O(dh^2)$ [39], Eq. (16) can be further simplified as

$$x_i = \frac{B_i}{\sum_{j\in\{A_{ij}\neq 0\}} A_{ij}} \tag{17}$$

The hydrodynamic forces exerted on the solid domain by the ambient fluid are evaluated with the velocity correction, which can be given as:

$$\boldsymbol{F}_H = \left(F_x, F_y, F_z\right) = -\sum_l \frac{\rho_f\delta\boldsymbol{u}_B^l\Delta s^l}{\Delta t} + \rho_f V_s\frac{\Delta\boldsymbol{U}_s}{\Delta t}, \tag{18}$$

where V_s and $\boldsymbol{U}_s$ denote the volume of the solid domain and the velocity of the mass center, respectively. In addition to hydrodynamic forces, the averaged Nusselt number is also important to quantify the heat transfer rate of the solid domain. The averaged Nusselt number on the surface of the solid domain is obtained from the temperature corrections [26], as follow:

$$\overline{Nu} = \frac{1}{S\left(T_s - T_{ref}\right)\chi}\sum_{l=1}^{N}\frac{\delta T_B^l\Delta s^l}{\Delta t}, \tag{19}$$

where S and T_s represent the surface area and the temperature of the immersed body; T_{ref} is the reference temperature.

3. Results and discussion

In this section, the numerical accuracy of EIB-RTLFS is being evaluated on the transient heat diffusion of a Gaussian hill. Subsequently, the robustness, computational efficiency, and suitability of our proposed method are evaluated through several benchmarks. Finally, the TFSI framework is coupled with the governing equation of a membrane structure [62] to demonstrate its capability in solving a fully coupled thermal–fluid–structure multi-physics system.

3.1. Numerical test of overall accuracy

The transient heat diffusion of a Gaussian hill is used in this section to test the overall accuracy of the EIB-RTLBFS. The 2D square computational domain has a length of $2L$ with uniform Eulerian mesh and periodic boundary condition on all four domain boundaries. A circular cylinder of radius $0.25L$ is placed at the center (L, L) of the domain, and the velocity and temperature on the boundary of the immersed cylinder are described by the analytical solutions. The initial velocity field of this particular problem is set such that $\mathbf{u} = (u_0, 0)$ and the initial isotherm is characterized by the following Gaussian distribution:

$$T(\mathbf{x}, 0) = \frac{T_{ref}}{2\pi\sigma^2}\exp\left[\frac{-\left(\mathbf{x} - \mathbf{X}_0\right)^2}{2\sigma^2}\right], \tag{20}$$

where T_{ref} denotes the reference temperature and σ is a constant. $\mathbf{X_0}$ denotes the center of the Gaussian hill. In this study, the parameters

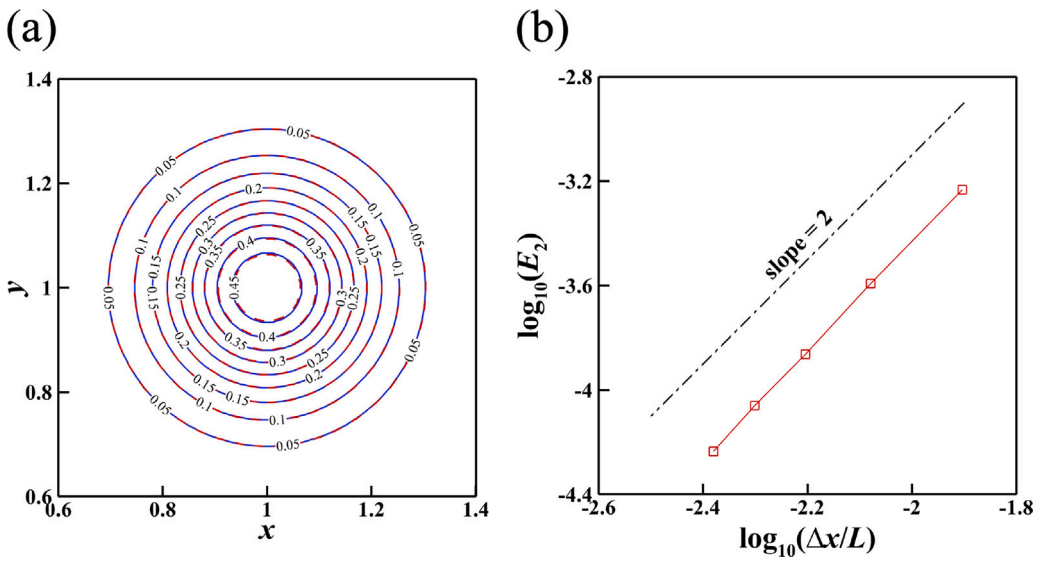

Fig. 2. The numerical accuracy test of the proposed EIB-RTLBFS by the transient heat diffusion of a Gaussian hill. (a) Comparison of the isotherms of predicted results (red dash line) and analytical solution (blue solid line) at $F_o = 0.005$.(b) Convergence of numerical error versus mesh spacing for unsteady heat diffusion of a Gaussian hill, indicating that the overall accuracy of the EIB-RTLBFS is of second-order.

$\sigma = 0.05L, T_{ref} = 2\pi\sigma^2, \mathbf{X}_0 = (0.5L, 0)$ are adopted. The analytical solution of the temperature distribution are given as follows:

$$T(\mathbf{x},t) = \frac{T_0}{2\pi\left(2\chi t+\sigma^2\right)}\exp\left[\frac{-\left(\mathbf{x}-\mathbf{X}_0-\mathbf{u}t\right)^2}{2\left(2\chi t+\sigma^2\right)}\right]. \tag{21}$$

The parameters $\Delta t = 1, \Delta x = L/50$, and the Peclect number $Pe = u_0 L/\chi = 100$ are applied. The numerical result obtained from EIB-RTLBFS is compared with the analytical solution obtained through Eq. 2 at isotherms corresponding to Fourier number $F_o = t\chi/L^2 = 0.005$, as shown in Fig. 2(a). It is evident from Fig. 2(a) that the predicted results by EIB-RTLBFS agree well with the analytical results.

Subsequently, 5 different sets of uniform mesh, namely 80^2, 120^2, 160^2, 200^2, and 240^2, with identical parameters of $\Delta t = 1$, and $Pe = 100$ are applied to investigate the convergence order. The relative error E_2 quantified by L_2 norm are calculated at $F_o = 0.005$ through the following expression:

$$E_2 = \sqrt{\frac{\sum_{i=1}^{N_0}\left(T_{numerical}-T_{exact}\right)^2}{N_0}}, \tag{22}$$

where N_0 denotes the total grid number of Eulerian mesh. The subscripts, numerical and exact, found in T denote the numerical results and analytical solutions, respectively. As shown in Fig. 2(b), the overall accuracy of the EIB-RTLBFS is of second-order in space. In addition, the results demonstrate that the EIB has negligible effects on the global accuracy of the RTLBFS.

3.2. Mixed heat transfer from a heated circular cylinder

To examine the capability of the EIB-RTLBFS for the mixed heat transfer in unsteady TFSI problems, an isothermal heated circular cylinder with a higher temperature of T_h fixed in the flow domain is considered in this subsection. The problem is governed by the dimensionless group: the Reynolds number (Re), the Prandtl number (Pr), the Grashof number (Gr), and the Richardson number (Ri), which are defined as:

$$Re = \frac{U_\infty D}{\nu}, \tag{23a}$$

$$Pr = \frac{\nu}{\chi}, \tag{23b}$$

Table 1
Comparison of representative properties at $Ri = 0$ and $Re = 100$, including the averaged Nusselt numbers and the strouhal number $St = fD/U_\infty$.

	$\overline{Nu}$	St
Hatton et al. [63] (experiment)	5.122	–
Shi et al. [64]	5.142	0.164
Wang et al. [58]	5.137	0.163
Chen et al. [26]	5.181	0.167
Present	**5.176**	**0.164**

$$Gr = \frac{g\zeta D^3\left(T_h - T_\infty\right)}{\nu^2}, \tag{23c}$$

$$Ri = \frac{Gr}{Re^2}, \tag{23d}$$

respectively. U_∞ denotes the flow velocity of the free stream and T_∞ denotes the temperature of the free stream. D is the diameter of the heated circular cylinder. In this test, the parameters $Pr = 0.7$ and $Re = 100$ are adopted, and three typical Richardson numbers are chosen to investigate the effects of the buoyancy force, namely, 0, 0.1, and 0.5. In addition, the computational domain is set as $[-50D, 50D]\times[-50D, 50D]$ with a mesh size of 500×500, where the flow region around the heated cylinder $[-0.8D, 0.8D] \times [-0.8D, 0.8D]$ is discretized uniformly with a mesh spacing of $\Delta x = 0.01D$.

Fig. 3 shows the comparisons between the streamlines and the isotherms of the mixed heat transfer from a heated circular cylinder provided by Wang et al. [58] and the present results at three different Richardson numbers. It can be seen that the results obtained by the proposed EIB-RTLBFS agree well with that of Wang et al. [58]. It is well known that unsteady flow starts to develop as the Reynolds number exceeds 100, which is consistent with our numerical results simulated at $Ri = 0$ (see Figs. 3(a) and 3(b)). As Richardson number increases, the natural convection emerges and stabilizes the unsteady flow. Hence, when Ri reaches 0.5, the fluctuations in the flow are suppressed and steady flow pattern is maintained (see Figs. 3(e) and 3(f)). These results are in consistent with previous studies [26,58], which qualitatively demonstrate the capability of the EIB-RTLBFS for simulating the heat transfer in unsteady TFSI problems.

The capability of EIB-RTLBFS in predicting unsteady flows is further tested by comparing the averaged Nusselt and Strouhal numbers of the

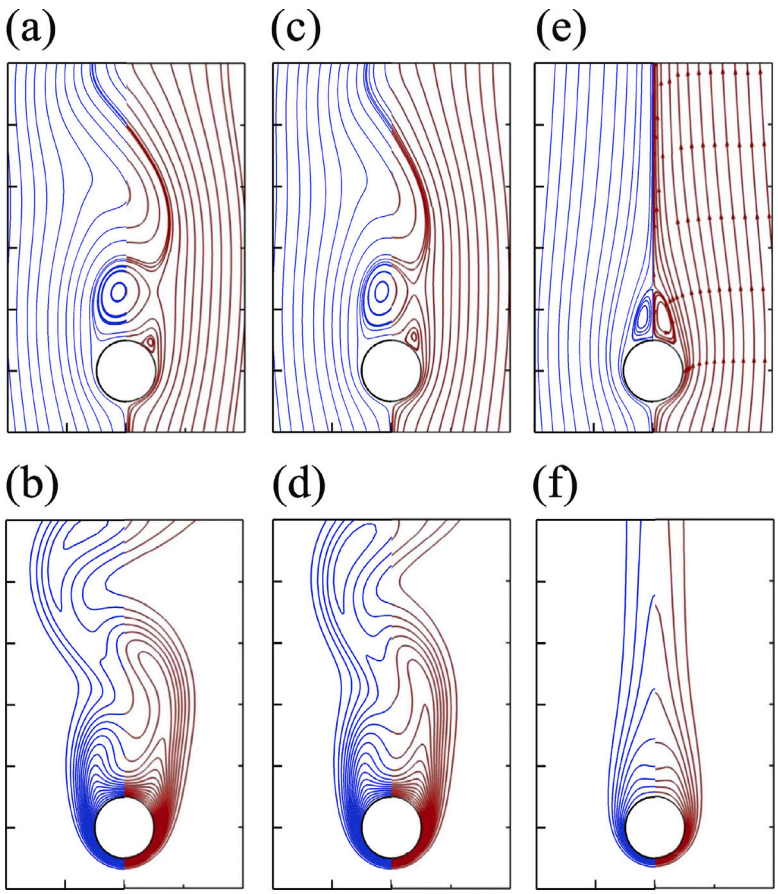

Fig. 3. Comparisons between instantaneous streamlines (top row) and isotherms (bottom row) of the mixed heat transfer from a heated circular cylinder provided by Wang et al. [58] (right part of each figure with red line) and the present results (left part of each figure with blue line) at $Re = 100$ and three different Richardson numbers, namely, $Ri = 0$ ($t/T = 0.625$, left column), $Ri = 0.1$ ($t/T = 0.625$, middle column) and $Ri = 0.5$ (steady, right column). As Richardson number increases, the natural convection emerges and stabilizes the unsteady flow. Hence, when Ri reaches 0.5, the fluctuations in the flow are suppressed and steady flow pattern is maintained. All cases show that the present results obtained by the proposed EIB-RTLBFS agree well with that of Wang et al. [58].

case without buoyancy force at $Ri = 0$ in this study with that of previous works [26,58,63,64]. It is evident from Table 1 that the present results agree well with the reference data, indicating the suitability of the EIB-RTLBFS for simulating unsteady thermal flows.

3.3. Natural convection around an inner heated sphere in a cubic enclosure

A 3D stationary inner heated sphere in a cubic enclosure is considered in this section to test the capability of the present solver for three-dimensional natural convection. As shown in Fig. 4, a heated inner sphere with radius $r = 0.2L$ is located in the center of a cubic enclosure with a length of L. The temperature on the spherical surface is assumed to be isothermal at T_h, and the temperature of the six cold walls of the cubic cavity is maintained at T_c. This problem is governed by the Rayleigh number Ra and the Prandtl number Pr, which are defined as:

$$\mathrm{Ra} = \frac{\zeta g \left(T_h - T_c\right) L^3}{\nu \chi} = \frac{U_c^2 L^2}{\nu \chi}, \tag{24a}$$

$$\mathrm{Pr} = \frac{\nu}{\chi}, \tag{24b}$$

where $U_c = \sqrt{\zeta g \left(T_h - T_c\right) L}$ denotes the characteristic velocity and it should satisfy the low Mach number limit. The reference temperature is set as $T_{ref} = \frac{(T_h + T_c)}{2}$. In the present test, the Prandtl number is set as $Pr = 0.7$ and the Rayleigh number is varied from 10^3 to 10^6. Similar to previous work [26], a uniform Cartesian mesh with the size of 80^3 is created for Ra = 10^3 and 10^4, while the mesh size is further

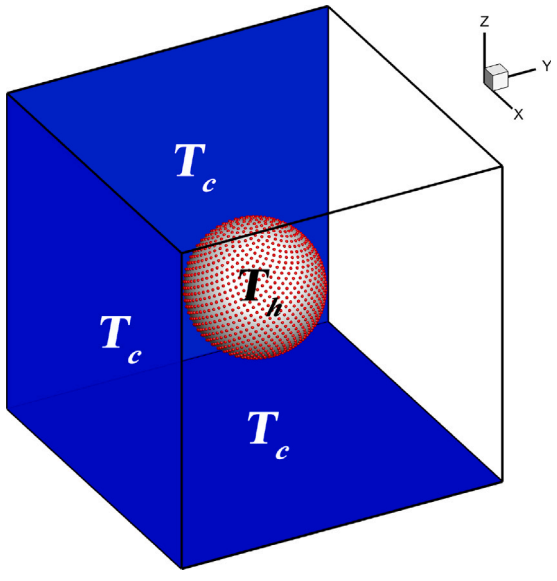

Fig. 4. Schematic view of the natural convection around an inner heated sphere in a cubic enclosure, where the temperature of the heated spherical surface is set as T_h and the temperatures on six cold walls of the cubic cavity are set as T_c. The red points on the spherical surface denote the distribution of Lagrangian points.

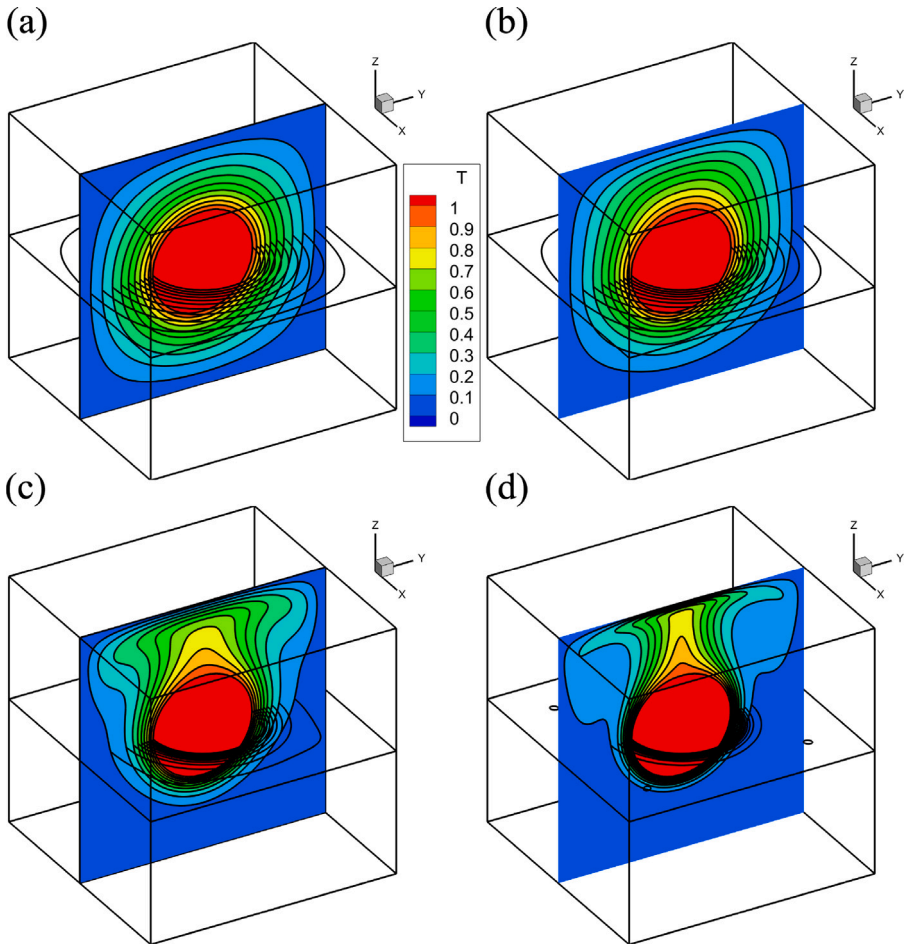

Fig. 5. Isotherms on the x-mid plane and the z-mid plane in natural convection around an inner heated sphere in a cubic cavity at different Rayleigh numbers, (a) Ra = 10^3, (b) Ra = 10^4, (c) Ra = 10^5, (d) Ra = 10^6. With the increasing of the Rayleigh number, the thermal expansion effect is enhanced and the isotherms on the z-mid plane are more squeezed towards the spherical surface.

refined to 200^3 for Ra = 10^5 and 10^6. To distribute the Lagrangian points (red points in Fig. 4) evenly on the spherical surface, the Fibonacci lattice [65] is adopted and the specific location of each Lagrangian point is defined as:

$$\varphi = \frac{2n-1}{N} - 1, \quad \xi = \frac{\sqrt{5}-1}{2}, \\ x_n = r\sqrt{1-\varphi^2}\cos(2\pi n\xi), \quad y_n = r\sqrt{1-\varphi^2}\sin(2\pi n\xi), \quad z_n = r\varphi, \tag{25}$$

where n and N denote the index of each Lagrangian point and the total number of the Lagrangian points, respectively. ξ is the golden ratio. It is worth mentioning here that the ratio of the maximum distance between adjacent Lagrangian points to the Eulerian mesh spacing in this work is always less than 1.6, ensuring that the EIB can establish a proper correlation between Lagrangian points and Eulerian meshes. In this study, the total number of Lagrangian points is the same as that of the previous work [26].

As shown in Fig. 5, the smooth isotherms on the x-mid and the z-mid planes can be predicted using our proposed solvers at all investigated Rayleigh numbers, demonstrating the stability of the newly devised solver in three-dimensional space at high Ra conditions. It is shown that the thermal expansion effect is enhanced as Rayleigh number increases, indicating that natural convection is stronger at higher Ra number. In addition, the isotherms on the z-mid plane are more squeezed towards the spherical surface as Ra number increases, and this is due to the enhancement in temperature gradient. Hence, the proposed method is capable of capturing the physics of natural convection, indicating the suitability of the proposed method for natural convection.

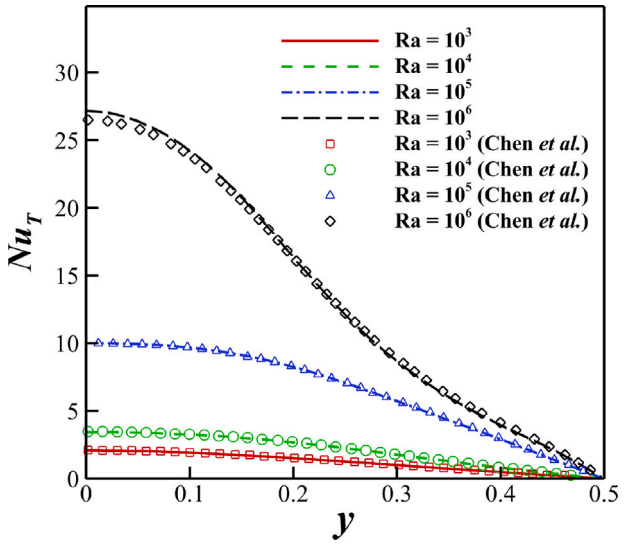

Fig. 6. The comparisons of the distribution of the local Nusselt number on the top wall's x-mid plane at different Rayleigh numbers. It quantitatively demonstrates that the present results obtained by EIB-RTLBFS agree with those in previous work [26], indicating the feasibility of the proposed solver.

In addition, quantitative comparisons of the local and averaged Nusselt numbers are performed to further assess the accuracy and

Table 2
Comparison of quantitative results, including the averaged Nusselt numbers on the top wall ($\overline{Nu}_T$), the bottom wall ($\overline{Nu}_B$), the side wall ($\overline{Nu}_S$) and the spherical surface ($\overline{Nu}_{Sp}$) and the difference of Nusselt number ($\Delta\overline{Nu}$).

Ra	Reference	$\overline{Nu}_T$	$\overline{Nu}_B$	$\overline{Nu}_S$	$\overline{Nu}_{Sp}$	$\Delta\overline{Nu}$
	Present	**0.707**	**0.621**	**0.662**	**7.907**	**−0.002**
Ra = 10^3	Yoon et al. [66]	0.69	0.62	0.66	7.42	−0.220
	Chen et al. [26]	0.711	0.626	0.667	7.973	0.003
	Present	**1.229**	**0.385**	**0.645**	**8.339**	**−0.002**
Ra = 10^4	Yoon et al.	1.23	0.38	0.64	7.80	−0.249
	Chen et al.	1.231	0.398	0.659	8.464	−0.01
	Present	**3.896**	**0.087**	**0.671**	**13.229**	**−0.017**
Ra = 10^5	Yoon et al.	3.87	0.08	0.67	12.61	−0.292
	Chen et al.	3.919	0.09	0.686	13.421	−0.007
	Present	**7.030**	**0.041**	**0.981**	**21.802**	**−0.036**
Ra = 10^6	Yoon et al.	6.97	0.04	0.97	20.64	−0.515
	Chen et al.	6.940	0.04	1.020	22.578	0.289

capability of the proposed method. Fig. 6 shows the local Nusselt numbers (Nu_T) along the x-midline on the top wall. It can be seen that the present results are in good agreement with those in previous work [26], demonstrating the feasibility of the EIB-RTLBFS. Various averaged Nusselt numbers are compared in Table 2, including the averaged Nusselt numbers on the top wall ($\overline{Nu}_T$), the bottom wall ($\overline{Nu}_B$), the side wall ($\overline{Nu}_S$), and the sphere's surface ($\overline{Nu}_{Sp}$). In addition, Chen et al. [26] pointed out that all the heat absorbed by the six walls of the cubic cavity should originate from the spherical surface, ensuring energy conservation. Hence, the ability of the present method in preserving energy conservation is evaluated based on the following equation:

$$\Delta\overline{Nu} = 4\pi r^2 \overline{Nu}_{Sp} - \left(\overline{Nu}_T + \overline{Nu}_B + 4\overline{Nu}_S\right) L^2, \tag{26}$$

and it is also tabulated in Table 2. As shown in Table 2, the averaged Nusselt numbers on the walls of the cubic cavity are in good agreement with those of previous studies [26,66]. However, there are some noticeable differences in the averaged Nusselt numbers on the spherical surface predicted by our proposed method and Yoon et al. [66], and this is attributed to the numerical errors of the predicted normal temperature gradient in Ref. [66]. Most importantly, the averaged Nusselt number differences ($\Delta\overline{Nu}$) of present work are the lowest when compared to previous works [26,66], especially in the case of Ra = 10^6. Therefore, Table 2 strongly demonstrated not only the accuracy of the EIB-RTLBFS, but also the superiority of the proposed method in preserving energy conservation.

3.4. Mixed convection of a heated rotating sphere in a cubic enclosure

To test the capability of the proposed method to capture the dynamic response of 3D moving boundary TFSI problems, a vertical rotating sphere (rotating axis is along the z-direction in Fig. 4) in a concentric cubical enclosure is considered in this section. In this test, the physical domain size is the same as that described in Section 3.3. The Prandtl number and the Rayleigh number are set as $Pr = 0.7$ and Ra = 10^4, respectively. Another important dimensionless parameter is the rotational Reynolds number $Re_w = \omega r L/\nu$ (ω denotes the rotational speed), which varies from 50 to 300 with an interval of 50 in this test. The mesh size of 250^3 is adopted in this study to be consistent with the previous study [27], and the total number of Lagrangian points is set to be 14,000.

Fig. 7 shows the 3D iso-surfaces and isotherms on the x-mid and z-mid plane at different rotational Reynolds numbers. The heat transfer is initially dominated by the convection and subsequently being dominated by the rotating behavior as Re_w increases. In addition, the rotational behavior is shown in Fig. 7 to induce an extra centrifugal transport behavior of the fluid, causing the iso-surfaces to be stretched

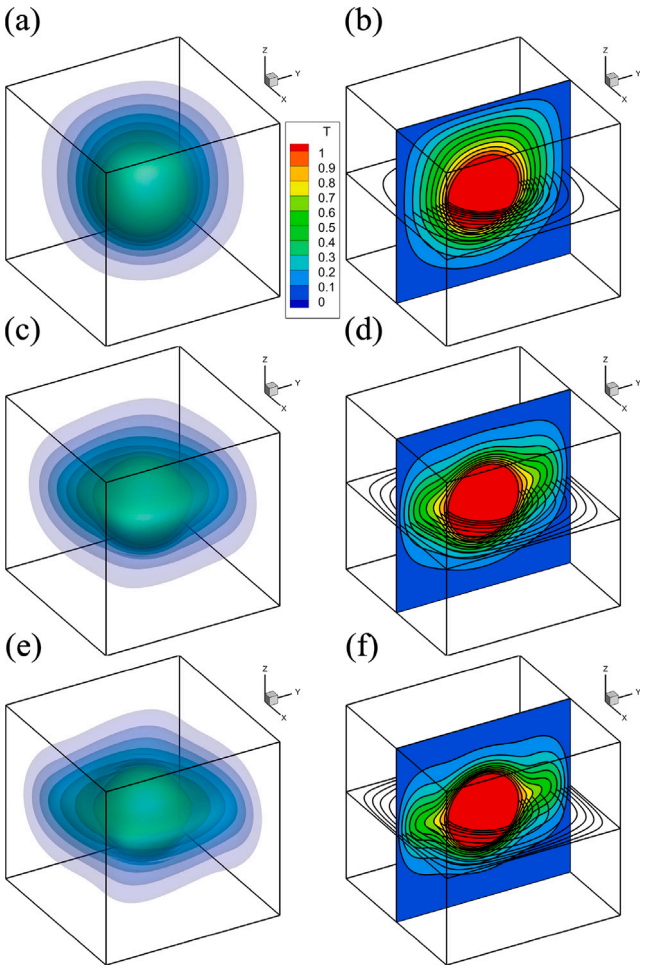

Fig. 7. 3D isosurfaces (left column) and isotherms on the x-mid and z-mid planes (right column) of the mixed convection between an inner heated rotating sphere and outer cubic cavity at Ra = 10^4 with different rotational Reynolds numbers; (a) and (b) Re_w = 50; (c) and (d) Re_w = 200; (e) and (f) Re_w = 300. As the rotational Reynolds number increases, the extra centrifugal transport behavior of the fluid enhances the heat transport along the horizontal direction.

in the horizontal plane, enhancing the heat transport along the horizontal direction. These observations are consistent with the previous study [27], which qualitatively demonstrates the capability of the EIB-RTLBFS for simulating the TFSI problems with moving boundaries.

The relative differences of the averaged Nusselt numbers on the walls and spherical surface are compared with previous work [27] in Fig. 8 at different rotational Reynolds numbers to further quantitatively evaluate the accuracy and robustness of EIB-RTBLFS. It can be seen that the present computational results on the walls of the cavity and the spherical surface agree well with the reference data in [27]. As rotational Reynolds number increases, the dominant component in the heat transfer switches from buoyancy force to centrifugal force, suppressing the heat transfers on the top and the bottom walls and enhancing the heat transfer on the side walls (see Fig. 8).

4. Heat transfer of a 3D heated flexible membrane structure

The heated flapping membrane structures are ubiquitous in engineering application with specific heat transfer demands [67]. In this section, the proposed EIB-RTLBFS solver is applied to simulate a 3D heated flexible membrane structure in a uniform flow to verify the accuracy and capability of the proposed method, where the TFSI problem introduced in this subsection involves large deformations,

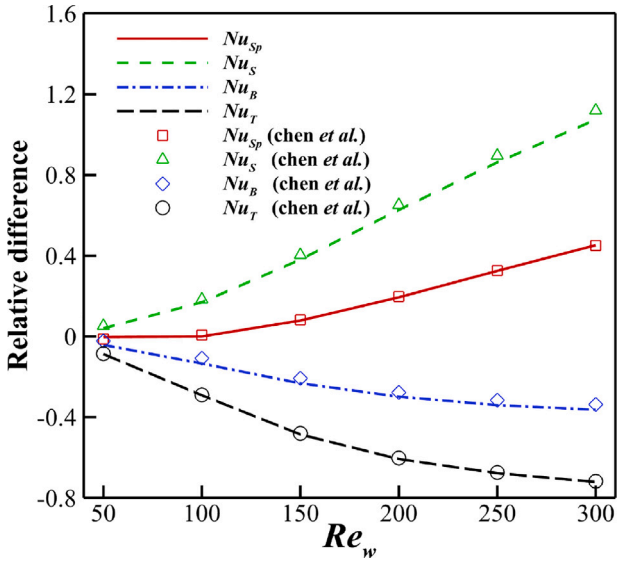

Fig. 8. Relative differences of the averaged Nusselt numbers on spherical surface and cavity walls between the case with a rotating sphere and the case with a stationary sphere at Ra = 10^4 with different rotational Reynolds numbers. With the increase of Re_w, the dominant component in the heat transfer switches from buoyancy force to centrifugal force, suppressing the heat transfers on the top and the bottom walls and enhancing the heat transfer on the side walls.

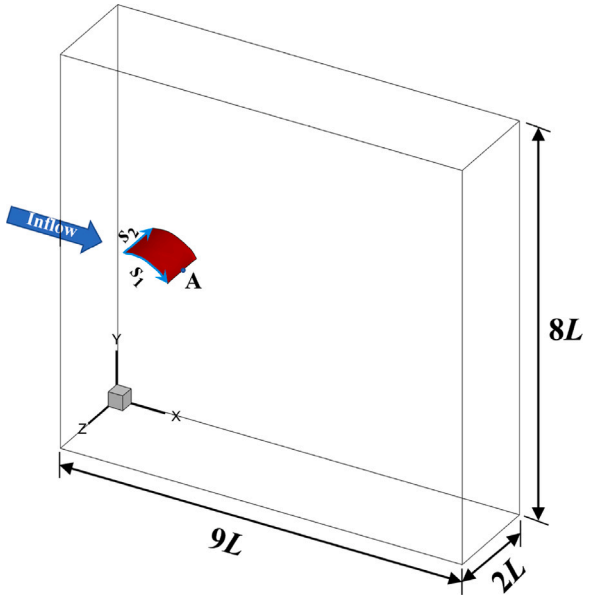

Fig. 9. Schematic view of the 3D isothermal heated membrane structure in a uniform flow, where a curvilinear coordinate system is formed along the s_1 and s_2 directions. Point A denote the midpoint on the trailing edge.

moving boundaries, and heat transfer, making it an ideal case to test the feasibility of the proposed method to solve a fully coupled thermal–fluid–structure multi-physics system.

4.1. Problem description and numerical setup

Fig. 9 shows the schematic view of a heated square membrane structure with length L in a uniform flow, where the midpoint of the leading edge is at the origin of the domain. The governing equation of the 3D isothermal membrane structure is specified in a curvilinear coordinate form [62] as follows:

$$\rho_s \frac{\partial^2 \mathbf{X}}{\partial t^2} = \sum_{i,j=1}^{2} \left[\frac{\partial}{\partial s_i} \left(\sigma_{ij} \frac{\partial \mathbf{X}}{\partial s_j} \right) - \frac{\partial^2}{\partial s_i \partial s_j} \left(\kappa_{ij}^b \frac{\partial^2 \mathbf{X}}{\partial s_i \partial s_j} \right) \right] + \boldsymbol{F}_H, \tag{27}$$

where $\mathbf{X}$ denotes the position of the Lagrangian points distributed on the flexible membrane structure and $\boldsymbol{F}_H$ is the hydrodynamic force exerted by the ambient fluid. ρ_s denotes the area density of the heated membrane structure, and σ_{ij} is defined as

$$\sigma_{ij} = \varphi_{ij} \left(\frac{\partial \mathbf{X}}{\partial s_i} \cdot \frac{\partial \mathbf{X}}{\partial s_j} - \Gamma_{ij}^0 \right), \tag{28a}$$

$$\Gamma_{ij}^0 = \begin{cases} 1, if\ i = j, \\ 0, if\ i \neq j. \end{cases} \tag{28b}$$

where $i = j$ or $i \neq j$, φ_{ij}, and κ_{ij}^b represent either tension and bending coefficients or shearing and twisting coefficients, respectively. Details on solving the governing equation Eq. (27) can be found in Appendix.

The problem is governed by the following dimensionless group: the Reynolds number $Re = U_\infty L/\nu$, the Prandtl number $Pr = \nu/\chi$, the Grashof number $Gr = g\zeta D^3 \left(T_h - T_\infty\right)/\nu^2$, the Richardson number $Ri = Gr/Re^2$, the mass ratio $\Theta = \rho_s/(\rho L)$, the dimensionless stretching and shearing coefficients $\Phi_{ij} = \varphi_{ij}/(\rho_s U_\infty^2)$, and the dimensionless bending and twisting coefficients $K_{ij} = \kappa_{ij}^b/(\rho_s U_\infty^2 L^2)$. The parameters: $Re = 200$, $Pr = 0.71$, $Ri = 0$, $\Theta = 1$, $\Phi_{11} = \Phi_{22} = 10^3$, $\Phi_{12} = 10$, $K_{11} = K_{22} = K_{12} = 10^{-4}$ are adopted in this problem. The overview of this TFSI problem is illustrated in Fig. 9, where the computational domain dimensions along x, y, and z direction are $[-2L, 7L]$, $[-4L, 4L]$, and $[-1L, 1L]$, respectively. A uniformly discretized finer mesh region of $[-0.2L, 1.3L] \times [-0.7L, 0.7L] \times [-0.7L, 0.7L]$ with $\Delta x_{fluid} = L/75$ is added near the solid domain and the wake region to ensure that all relevant physics are captured at a reduced computational cost. It should be noted that the leading edge is pinned and the free moving boundary condition is applied at the other three edges. The Lagrangian points are evenly distributed on the membrane structure, where $\Delta x_{solid} = L/50$. The temperature on the membrane structure's surface is assumed to be isothermal at $T_h = 1$. Dirichlet boundary conditions ($u = U_\infty$, $v = w = T_\infty = 0$) are applied at the inflow boundary and the Neumann boundary conditions ($\partial \mathbf{u}/\partial n = 0, \partial T/\partial n = 0$) are implemented at the outflow boundary and the four side walls.

4.2. Numerical results of the 3D heated membrane structure

Fig. 10 shows the instantaneous vortical structures, temperature iso-surface, isotherm on the z-mid plane, and the flapping profile of the heated flapping membrane structure. It can be seen that the hairpin-like vortical structures emerge, which is consistent with the previous studies [62,68,69]; and the temperature iso-surface concentrates around the vortical structures generated by the heated membrane structure. These numerical observations are consistent with the physical mechanism, qualitatively validating the feasibility of the EIB-RTLBFS for predicting the nonlinear characteristics of a fully coupled thermal–fluid–structure systems.

Quantitative results, including the transverse displacement of the midpoint A on the trailing edge (see Fig. 9), averaged Nusselt number of the membrane structure, drag coefficient, and lift coefficient, are shown in Fig. 11. The numerical results generated by the EIB-RTLBFS are in good agreement with that of the previous studies [62,68–70], demonstrating the feasibility of the EIB-RTLBFS for solving TFSI problems. Besides, the time history of the averaged Nusselt number of the heated membrane structure shows that the heat transfer rate is enhanced when the trailing edge is at the absolute maximum amplitude along the y-direction. In contrast, the heat transfer rate is at its lowest rate when the trailing edge is around the neutral position. The observed phenomenon is due to the fact that the heat transfer rate is closely related to the projected area of the heated membrane structure perpendicular to the streamwise direction.

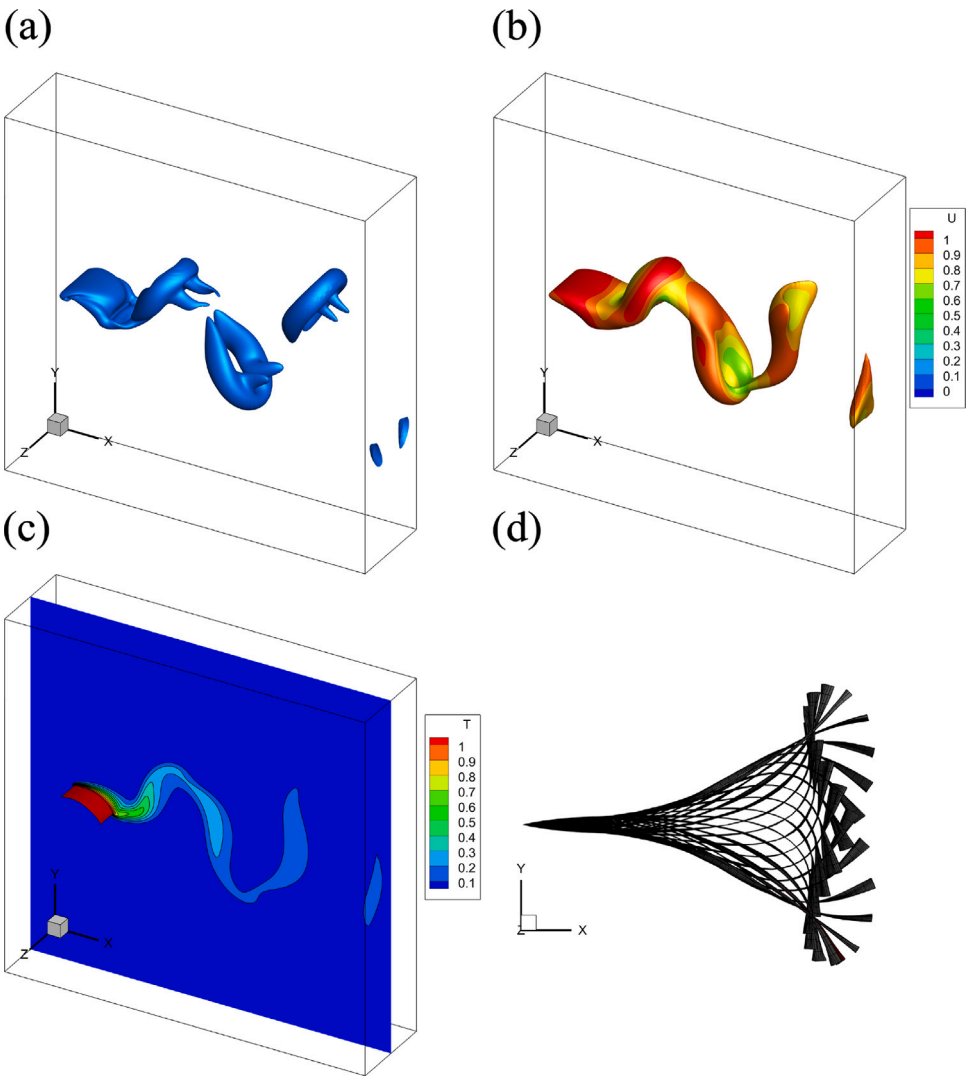

Fig. 10. Instantaneous (a) vorticity structures (which is visualized by the iso-surface of $Q = 0.2$), (b) iso-surface of $T = 0.1$ colored by the streamwise velocity, and (c) isotherm on the z-mid plane for the heated flapping membrane structure at one time instance and $Re = 200$; (d) a side-view of the flapping profile of the heated membrane structure.

5. Conclusions

In this paper, we proposed a novel approach (EIB-RTLBFS) that is not only computational efficient, but also able to solve challenging problems found in thermal–fluid–structure interaction, for instance, the TFSI problem related to the flexible membrane structure. In this new approach, a fractional step method is utilized to resolve the N–S equations in two successive steps. Briefly, the RTLBFS predicts the intermediate flow field without considering the solid domain in the predictor step. Subsequently, the EIB is introduced to simultaneously evaluate the velocity and temperature corrections on the surface of the solid domain while ensuring that the Dirichlet boundary conditions are fully satisfied. It is noteworthy that the RTLBFS is a weakly compressible finite volume solver with a clear mechanism to achieve good numerical stability for high Rayleigh number thermal flows. In contrary to conventional IBM, the EIB method introduced in this work eliminates the needs to solve and invert a large correlation matrix, thereby, increasing the computational efficiency in handling the TFSI coupling process. Therefore, the proposed approach inherited the advantages found in both the EIB and RTLBFS solvers, allowing us to solve complex TFSI problems accurately and efficiently.

The numerical accuracy-test demonstrates that the EIB-RTLBFS is second-order accuracy in space. Four typical TFSI problems, including unsteady flow, natural convection, moving boundary, and large deformation, are numerically studied with the proposed method, and the predicted results are compared with previous studies. The good agreement between the numerical results generated by EIB-RTLBFS and previous works verifies the feasibility and robustness of the EIB-RTLBFS. Most importantly, the EIB-RTLBFS is found to have better energy conservation ability than previous numerical methods used in Refs. [26,66]. Lastly, the proposed method is further tested on solving the heat transfer around a 3D heated flexible membrane structure, where our numerical results are in excellent agreement with other numerical methods, indicating its suitability for simulating fully coupled thermal–fluid–structure interaction problems. All in all, our study demonstrates that the EIB-RTLBFS is very suited for TFSI problems with large deformations and moving boundaries.

CRediT authorship contribution statement

Buchen Wu: Conceptualization, Methodology, Software, Validation, Writing – original draft. **Jinhua Lu:** Methodology, Writing – original draft. **HsuChew Lee:** Writing – original draft. **Chang Shu:** Formal analysis, Supervision, Writing – original draft. **Minping Wan:** Formal analysis, Supervision, Writing – original draft.

Declaration of competing interest

The authors declare that they have no known competing financial interests or personal relationships that could have appeared to influence the work reported in this paper.

Data availability

Data will be made available on request.

Acknowledgments

This work has been supported by the Key-Area Research and Development Program of Guangdong Province, China (Grant No. 2021B0101190003), the Department of Science and Technology of Guangdong Province, China (Grant No. 2020B1212030001), and the Shenzhen Science & Technology Program, China (Grant No. KQTD20180411143441009). Numerical simulations have been supported by the Center for Computational Science and Engineering of Southern University of Science and Technology.

Appendix. The methodology for the 3D membrane structure dynamics

In this work, the 3D flexible membrane structure is decomposed into a series of parallel flexible filaments along the x direction, and these filaments are connected along the z direction, similarly to the previous work [70]. $\mathbf{X}^* = 2\mathbf{X}^n - \mathbf{X}^{n-1}$ (an estimation of the new position) is introduced to simplify the updating process. For each filament, when $i = j$=1, the bending force term $\frac{\partial^2}{\partial s_1^2}\left(\kappa_{11}^b \frac{\partial^2 \mathbf{X}}{\partial s_1^2}\right)$, and stretching force term $\frac{\partial}{\partial s_1}\left(\Gamma \frac{\partial \mathbf{X}}{\partial s_1}\right)$ are regarded as the internal force terms; the other force terms are treated as external force terms. Therefore, Eq. (27) is simplified as

$$\rho_s \frac{\partial^2 \mathbf{X}}{\partial t^2} = \frac{\partial}{\partial s_1}\left(\Gamma \frac{\partial \mathbf{X}}{\partial s_1}\right) - \frac{\partial^2}{\partial s_1^2}\left(\kappa_{11}^b \frac{\partial^2 \mathbf{X}}{\partial s_1^2}\right) + \mathbf{F}_H + \boldsymbol{F}_{external}\left(\mathbf{X}^*\right), \quad \text{(A.1)}$$

where $\boldsymbol{F}_{external}(\mathbf{X}^*)$ represents the summation of the external force terms. The external force terms in three-dimensional flexible membrane structure governing equation (Eq. (A.1)) are obtained by [62]
for $i = j$=2,

$$\frac{\partial}{\partial s_2}\left(\sigma_{22} \frac{\partial \mathbf{X}^*}{\partial s_2}\right) = D_2^-\left(\sigma_{22} D_2^+ \mathbf{X}^*\right), \quad \text{(A.2)}$$

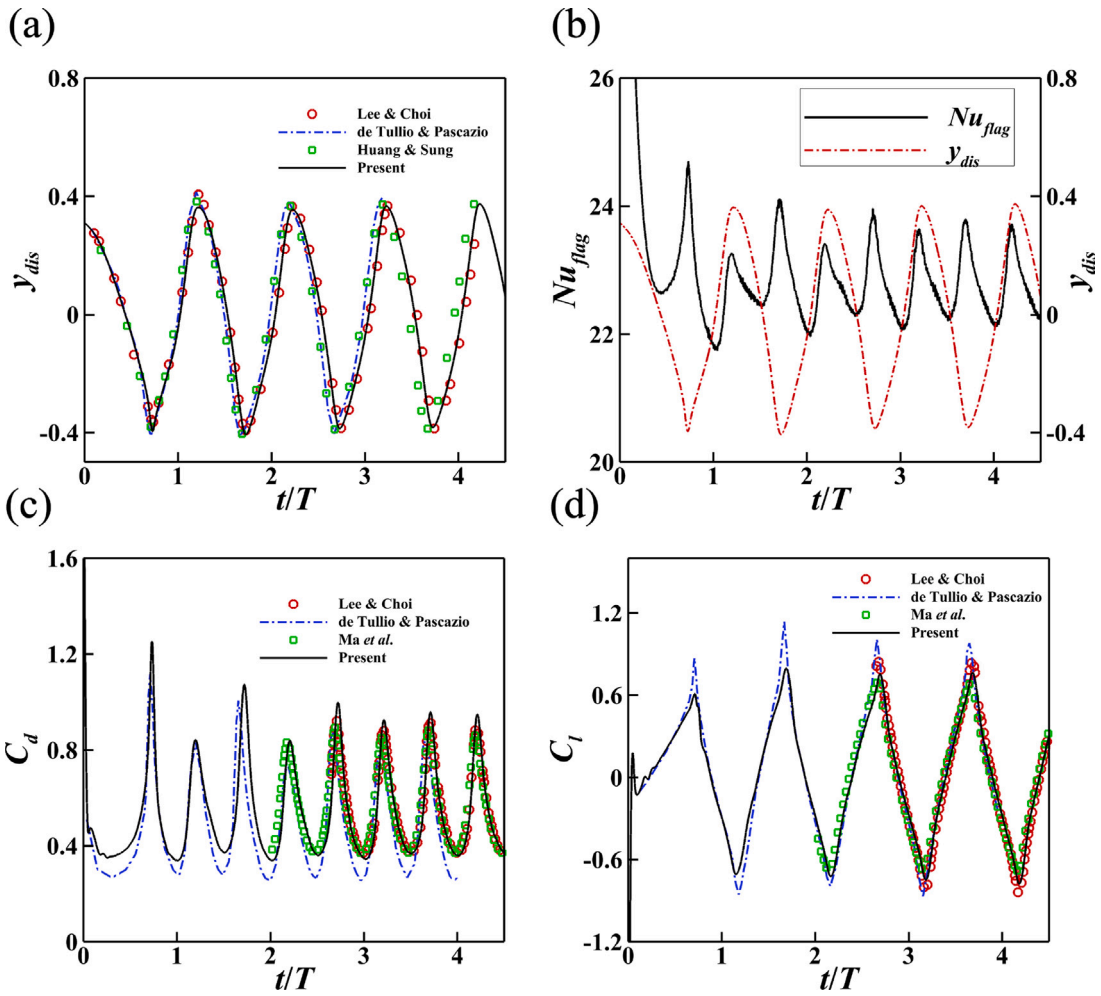

Fig. 11. Time histories of (a) the transverse displacement of point A (see Fig. 9), (b) the averaged Nusselt number of the heated membrane structure, (c) the drag coefficient $C_d = 2F_x/\rho U_\infty^2 L^2$, and (d) the lift coefficient $C_l = 2F_y/\rho U_\infty^2 L^2$. The transverse displacement is compared with that of Refs. [62,68,69], and the force coefficients are compared with the Reference data [68–70]. The numerical results generated by the EIB-RTLBFS agree well with that of the previous studies [62,68–70], demonstrating the feasibility of the EIB-RTLBFS for solving TFSI problems. The results in (b) indicates that the heat transfer rate is closely related to the projected area of the heated membrane structure perpendicular to the streamwise direction.

$$\frac{\partial^2}{\partial s_2^2}\left(\kappa_{22}^b \frac{\partial^2 \mathbf{X}^*}{\partial s_2^2}\right) = D_{22}^0\left(\kappa_{22}^b D_{22}^0 \mathbf{X}^*\right); \tag{A.3}$$

for i=1, j=2 or i=2, j=1,

$$\frac{\partial}{\partial s_1}\left(\sigma_{12}\frac{\partial \mathbf{X}^*}{\partial s_2}\right) = \frac{1}{2}\left[D_1^-\left(\sigma_{12}^+ D_2^+ \mathbf{X}^*\right) + D_1^-\left(\sigma_{12}^- D_2^- \mathbf{X}^*\right)\right], \tag{A.4}$$

$$\frac{\partial}{\partial s_2}\left(\sigma_{21}\frac{\partial \mathbf{X}^*}{\partial s_1}\right) = \frac{1}{2}\left[D_2^-\left(\sigma_{21}^+ D_1^+ \mathbf{X}^*\right) + D_2^-\left(\sigma_{21}^- D_1^- \mathbf{X}^*\right)\right], \tag{A.5}$$

$$\frac{\partial^2}{\partial s_1 s_2}\left(\kappa_{12}^b \frac{\partial^2 \mathbf{X}^*}{\partial s_1 s_2}\right) = \frac{\partial^2}{\partial s_2 s_1}\left(\kappa_{21}^b \frac{\partial^2 \mathbf{X}^*}{\partial s_2 s_1}\right) = D_{12}^-\left(\kappa_{12}^b D_{12}^+ \mathbf{X}^*\right). \tag{A.6}$$

In the above equations, based on the arc length s_1 and s_2, the downwind difference $\left[D_1^+\phi\right]_{i,j}$ and upwind difference $\left[D_1^-\phi\right]_{i,j}$, the second-order central difference $\left[D_{22}^0\phi\right]_{i,j}$, and the second-order cross difference $\left[D_{12}^+\phi\right]_{i,j}$, $\left[D_{12}^-\phi\right]_{i,j}$ are defined as

$$\begin{aligned}
&\left[D_1^+\phi\right]_{i,j} = \left(\phi_{i+1,j} - \phi_{i,j}\right)/\Delta s_1,\\
&\left[D_1^-\phi\right]_{i,j} = \left(\phi_{i,j} - \phi_{i-1,j}\right)/\Delta s_1,\\
&\left[D_{22}^0\phi\right]_{i,j} = \left(\phi_{i,j+1} - 2\phi_{i,j} + \phi_{i,j-1}\right)/\Delta s_1^2,\\
&\left[D_{12}^+\phi\right]_{i,j} = \left(\phi_{i+1,j+1} - \phi_{i+1,j} - \phi_{i,j+1} + \phi_{i,j}\right)/\left(\Delta s_1 \Delta s_2\right),\\
&\left[D_{12}^-\phi\right]_{i,j} = \left(\phi_{i,j} - \phi_{i,j-1} - \phi_{i-1,j} + \phi_{i-1,j-1}\right)/\left(\Delta s_1 \Delta s_2\right).
\end{aligned} \tag{A.7}$$

Then, the tensile stress Γ is obtained by the Poisson equation with the inextensibility condition

$$\begin{aligned}
&\frac{\partial \mathbf{X}}{\partial s_1}\cdot\frac{\partial^2}{\partial s_1^2}\left(\Gamma\frac{\partial \mathbf{X}}{\partial s_1}\right)\\
&= \frac{1}{2}\frac{\partial^2}{\partial t^2}\left(\frac{\partial \mathbf{X}}{\partial s_1}\cdot\frac{\partial \mathbf{X}}{\partial s_1}\right)\\
&- \frac{\partial^2 \mathbf{X}}{\partial t \partial s_1}\cdot\frac{\partial^2 \mathbf{X}}{\partial t \partial s_1} - \frac{\partial \mathbf{X}}{\partial s_1}\cdot\frac{\partial}{\partial s_1}\left[\frac{\partial^2}{\partial s_1^2}\left(\kappa_{11}^b\frac{\partial^2 \mathbf{X}}{\partial s_1^2}\right) + \boldsymbol{F}_H + \mathbf{F}_{external}\right].
\end{aligned} \tag{A.8}$$

Readers are referred to the work of Huang et al. [71] for more details on how tension force is obtained through Eq. (A.8). Eq. (A.1) is discretized by the implicit second-order finite-difference scheme, and the corresponding discretized form reads

$$\begin{aligned}
&\frac{\mathbf{X}^{n+1} - 2\mathbf{X}^n + \mathbf{X}^{n-1}}{\Delta t^2}\\
&= \frac{\partial}{\partial s_1}\left(\Gamma^{n+\frac{1}{2}}\frac{\partial \mathbf{X}^{n+1}}{\partial s_1}\right) - \frac{\partial^2}{\partial s_1^2}\left(\kappa_{11}^b\frac{\partial^2 \mathbf{X}^*}{\partial s_1^2}\right) + \mathbf{F}_H + \mathbf{F}_{external}\left(\mathbf{X}^*\right).
\end{aligned} \tag{A.9}$$

The updated position is obtained by solving Eq. (A.9).

References

[1] Kim B, Lee D, Ha M, Yoon H. A numerical study of natural convection in a square enclosure with a circular cylinder at different vertical locations. Int J Heat Mass Transfer 2008;51(7–8):1888–906.

[2] Wang Z, Fan J, Luo K, Cen K. Immersed boundary method for the simulation of flows with heat transfer. Int J Heat Mass Transfer 2009;52(19–20):4510–8.

[3] Deen NG, Kriebitzsch SH, van der Hoef MA, Kuipers J. Direct numerical simulation of flow and heat transfer in dense fluid–particle systems. Chem Eng Sci 2012;81:329–44.

[4] Deen NG, Peters E, Padding JT, Kuipers J. Review of direct numerical simulation of fluid–particle mass, momentum and heat transfer in dense gas–solid flows. Chem Eng Sci 2014;116:710–24.

[5] Hellenkamp M, Pfeifer H. Thermally induced stresses on radiant heating tubes including the effect of fluid–structure interaction. Appl Therm Eng 2016;94:364–74.

[6] Yun S, Kwon J, Lee D, Shin HH, Kim Y. Heat transfer and stress characteristics of additive manufactured FCCZ lattice channel using thermal fluid-structure interaction model. Int J Heat Mass Transfer 2020;149:119187.

[7] Shahabadi M, Mehryan S, Ghalambaz M, Ismael M. Controlling the natural convection of a non-Newtonian fluid using a flexible fin. Appl Math Model 2021;92:669–86.

[8] Beeby SP, Tudor MJ, White N. Energy harvesting vibration sources for microsystems applications. Meas Sci Technol 2006;17(12):R175.

[9] Al-Amiri A, Khanafer K, Bull J, Pop I. Effect of sinusoidal wavy bottom surface on mixed convection heat transfer in a lid-driven cavity. Int J Heat Mass Transfer 2007;50(9–10):1771–80.

[10] Mills ZG, Aziz B, Alexeev A. Beating synthetic cilia enhance heat transport in microfluidic channels. Soft Matter 2012;8(45):11508–13.

[11] Felicjancik J, Ziółkowski P, Badur J. An advanced thermal-FSI approach of an evaporation of air heat pump. Trans Inst Fluid-Flow Mach 2015;(129):111–41.

[12] Yan J, Yan W, Lin S, Wagner G. A fully coupled finite element formulation for liquid–solid–gas thermo-fluid flow with melting and solidification. Comput Methods Appl Mech Engrg 2018;336:444–70.

[13] Wu B, Laima S. Experimental study on characteristics of vortex-induced vibration of a twin-box girder and damping effects. J Fluids Struct 2021;103:103282.

[14] Hirt CW, Amsden AA, Cook J. An arbitrary Lagrangian-Eulerian computing method for all flow speeds. J Comput Phys 1974;14(3):227–53.

[15] Donea J, Giuliani S, Halleux J-P. An arbitrary Lagrangian-Eulerian finite element method for transient dynamic fluid-structure interactions. Comput Methods Appl Mech Engrg 1982;33(1–3):689–723.

[16] Andersen A, Pesavento U, Wang ZJ. Unsteady aerodynamics of fluttering and tumbling plates. J Fluid Mech 2005;541:65–90.

[17] Jin C, Xu K. Numerical study of the unsteady aerodynamics of freely falling plates. Commun Comput Phys 2008;3(4):834–51.

[18] Long T, Hu D, Wan D, Zhuang C, Yang G. An arbitrary boundary with ghost particles incorporated in coupled FEM–SPH model for FSI problems. J Comput Phys 2017;350:166–83.

[19] Long T, Yang P, Liu M. A novel coupling approach of smoothed finite element method with SPH for thermal fluid structure interaction problems. Int J Mech Sci 2020;174:105558.

[20] Long T, Huang C, Hu D, Liu M. Coupling edge-based smoothed finite element method with smoothed particle hydrodynamics for fluid structure interaction problems. Ocean Eng 2021;225:108772.

[21] Long T, Zhang Z, Liu M. Multi-resolution technique integrated with smoothed particle element method (SPEM) for modeling fluid-structure interaction problems with free surfaces. Sci China Phys Mech Astron 2021;64(8):1–22.

[22] Mittal R, Iaccarino G. Immersed boundary methods. Annu Rev Fluid Mech 2005;37:239–61.

[23] Ren W, Shu C, Wu J, Yang W. Boundary condition-enforced immersed boundary method for thermal flow problems with Dirichlet temperature condition and its applications. Comput & Fluids 2012;57:40–51.

[24] Liao C-C, Lin C-A. Simulations of natural and forced convection flows with moving embedded object using immersed boundary method. Comput Methods Appl Mech Engrg 2012;213:58–70.

[25] Soti AK, Bhardwaj R, Sheridan J. Flow-induced deformation of a flexible thin structure as manifestation of heat transfer enhancement. Int J Heat Mass Transfer 2015;84:1070–81.

[26] Chen Z, Shu C, Yang L, Zhao X, Liu N. Immersed boundary–simplified thermal lattice Boltzmann method for incompressible thermal flows. Phys Fluids 2020;32(1):013605.

[27] Chen Z, Yang L, Shu C, Zhao X, Liu N, Liu Y. Mixed convection between rotating sphere and concentric cubical enclosure. Phys Fluids 2021;33(1):013605.

[28] Al-Amiri A, Khanafer K. Fluid–structure interaction analysis of mixed convection heat transfer in a lid-driven cavity with a flexible bottom wall. Int J Heat Mass Transfer 2011;54(17–18):3826–36.

[29] Raisi A, Arvin I. A numerical study of the effect of fluid-structure interaction on transient natural convection in an air-filled square cavity. Int J Therm Sci 2018;128:1–14.

[30] Ghalambaz M, Jamesahar E, Ismael MA, Chamkha AJ. Fluid-structure interaction study of natural convection heat transfer over a flexible oscillating fin in a square cavity. Int J Therm Sci 2017;111:256–73.

[31] Ismael MA, Jasim HF. Role of the fluid-structure interaction in mixed convection in a vented cavity. Int J Mech Sci 2018;135:190–202.

[32] Beyer RP, LeVeque RJ. Analysis of a one-dimensional model for the immersed boundary method. SIAM J Numer Anal 1992;29(2):332–64.

[33] Peskin CS. Numerical analysis of blood flow in the heart. J Comput Phys 1977;25(3):220–52.

[34] Lai M-C, Peskin CS. An immersed boundary method with formal second-order accuracy and reduced numerical viscosity. J Comput Phys 2000;160(2):705–19.

[35] Feng Z-G, Michaelides EE. The immersed boundary-lattice Boltzmann method for solving fluid–particles interaction problems. J Comput Phys 2004;195(2):602–28.

[36] Feng Z-G, Michaelides EE. Proteus: a direct forcing method in the simulations of particulate flows. J Comput Phys 2005;202(1):20–51.

[37] Wu J, Shu C. Implicit velocity correction-based immersed boundary-lattice Boltzmann method and its applications. J Comput Phys 2009;228(6):1963–79.

[38] Wu J, Shu C. An improved immersed boundary-lattice Boltzmann method for simulating three-dimensional incompressible flows. J Comput Phys 2010;229(13):5022–42.

[39] Zhao X, Chen Z, Yang L, Liu N, Shu C. Efficient boundary condition-enforced immersed boundary method for incompressible flows with moving boundaries. J Comput Phys 2021;110425.

[40] Wu B, Shu C, Wan M, Wang Y, Chen S. Hydrodynamic performance of an unconstrained flapping swimmer with flexible fin: A numerical study. Phys Fluids 2022;34(1):011901.

[41] Wu B, Shu C, Lee H, Wan M. The effects of caudal fin's bending stiffness on a self-propelled carangiform swimmer. Phys Fluids 2022;34(4):041901.

[42] Eymard R, Gallouët T, Herbin R. Finite volume methods. In: Handbook of numerical analysis. Vol. 7. Elsevier; 2000, p. 713–1018.
[43] Thomas JW. Numerical partial differential equations: finite difference methods. Vol. 22. Springer Science & Business Media; 2013.
[44] Reddy JN, Gartling DK. The finite element method in heat transfer and fluid dynamics. CRC Press; 2010.
[45] Kim J, Moin P. Application of a fractional-step method to incompressible Navier-Stokes equations. J Comput Phys 1985;59(2):308–23.
[46] Van Kan J. A second-order accurate pressure-correction scheme for viscous incompressible flow. SIAM J Sci Stat Comput 1986;7(3):870–91.
[47] Bell JB, Colella P, Glaz HM. A second-order projection method for the incompressible Navier-Stokes equations. J Comput Phys 1989;85(2):257–83.
[48] McNamara G, Alder B. Analysis of the lattice Boltzmann treatment of hydrodynamics. Physica A 1993;194(1–4):218–28.
[49] Chen Y, Ohashi H, Akiyama M. Thermal lattice Bhatnagar-Gross-Krook model without nonlinear deviations in macrodynamic equations. Phys Rev E 1994;50(4):2776.
[50] Chen Y, Ohashi H, Akiyama M. Two-parameter thermal lattice BGK model with a controllable Prandtl number. J Sci Comput 1997;12(2):169–85.
[51] McNamara GR, Garcia AL, Alder BJ. A hydrodynamically correct thermal lattice Boltzmann model. J Stat Phys 1997;87(5):1111–21.
[52] Filippova O, Hänel D. A novel lattice BGK approach for low mach number combustion. J Comput Phys 2000;158(2):139–60.
[53] Lallemand P, Luo L-S. Theory of the lattice Boltzmann method: Acoustic and thermal properties in two and three dimensions. Phys Rev E 2003;68(3):036706.
[54] Mezrhab A, Bouzidi M, Lallemand P. Hybrid lattice-Boltzmann finite-difference simulation of convective flows. Comput & Fluids 2004;33(4):623–41.
[55] Verhaeghe F, Blanpain B, Wollants P. Lattice Boltzmann method for double-diffusive natural convection. Phys Rev E 2007;75(4):046705.
[56] He X, Chen S, Doolen GD. A novel thermal model for the lattice Boltzmann method in incompressible limit. J Comput Phys 1998;146(1):282–300.
[57] Guo Z, Zheng C, Shi B, Zhao T. Thermal lattice Boltzmann equation for low mach number flows: Decoupling model. Phys Rev E 2007;75(3):036704.
[58] Wang Y, Shu C, Teo C. Thermal lattice Boltzmann flux solver and its application for simulation of incompressible thermal flows. Comput & Fluids 2014;94:98–111.
[59] Wang Y, Shu C, Teo CJ, Wu J, Yang L. Three-dimensional lattice Boltzmann flux solver and its applications to incompressible isothermal and thermal flows. Commun Comput Phys 2015;18(3):593–620.
[60] Lu J, Dai C, Yu P. The reconstructed thermal lattice Boltzmann flux solver and its applications for simulations of thermal flows. 2022, arXiv preprint arXiv:2202.13449.
[61] Lu J, Lei H, Shu C, Dai C. The more actual macroscopic equations recovered from lattice Boltzmann equation and their applications. J Comput Phys 2020;415:109546.
[62] Huang W-X, Sung HJ. Three-dimensional simulation of a flapping flag in a uniform flow. J Fluid Mech 2010;653:301.
[63] Hatton A, James D, Swire H. Combined forced and natural convection with low-speed air flow over horizontal cylinders. J Fluid Mech 1970;42(1):17–31.
[64] Shi J-M, Gerlach D, Breuer M, Biswas G, Durst F. Heating effect on steady and unsteady horizontal laminar flow of air past a circular cylinder. Phys Fluids 2004;16(12):4331–45.
[65] González Á. Measurement of areas on a sphere using fibonacci and latitude–longitude lattices. Math Geosci 2010;42(1):49–64.
[66] Yoon H, Yu D, Ha M, Park Y. Three-dimensional natural convection in an enclosure with a sphere at different vertical locations. Int J Heat Mass Transfer 2010;53(15–16):3143–55.
[67] Solano T, Ordonez JC, Shoele K. Flapping dynamics of a flag in the presence of thermal convection. J Fluid Mech 2020;895.
[68] Lee I, Choi H. A discrete-forcing immersed boundary method for the fluid–structure interaction of an elastic slender body. J Comput Phys 2015;280:529–46.
[69] de Tullio MD, Pascazio G. A moving-least-squares immersed boundary method for simulating the fluid–structure interaction of elastic bodies with arbitrary thickness. J Comput Phys 2016;325:201–25.
[70] Ma J, Wang Z, Young J, Lai JC, Sui Y, Tian F-B. An immersed boundary-lattice Boltzmann method for fluid-structure interaction problems involving viscoelastic fluids and complex geometries. J Comput Phys 2020;415:109487.
[71] Huang W-X, Shin SJ, Sung HJ. Simulation of flexible filaments in a uniform flow by the immersed boundary method. J Comput Phys 2007;226(2):2206–28.